Agent-Based Modeling Demonstrates How Local Chemotactic Behavior Can Shape Biofilm Architecture

Emily G. Sweeney[a], Andrew Nishida[b,1], Alexandra Weston[a,2], Maria S. Bañuelos[a], Kristin Potter[c,3], John Conery[b], Karen Guillemin[a,d,*]

[a]Institute of Molecular Biology, University of Oregon, Eugene, Oregon 97403, United States

[b]Institute of Ecology and Evolution, University of Oregon, Eugene, Oregon 97403, United States

[c]College of Arts and Sciences Information Technology, University of Oregon, Eugene, Oregon 97403, United States

[d]Humans and the Microbiome Program, Canadian Institute for Advanced Research, Toronto, Ontario M5G 1Z8, Canada

[1]Current address: Altius Institute, 2211 Elliott Ave., 4th floor, Seattle, Washington 98121, United States

[2]Current address: Memorial Sloan Kettering Cancer Center, 885 2nd Ave, 6th floor, New York, New York 10017, United States

[3]Current address: National Renewable Energy Laboratory, 15257 Denver West Parkway, Golden, Colorado 80401, United States

[*]Corresponding author: phone (541) 346-5360, email kguillem@uoregon.edu

Abstract: Mature bacterial biofilms have elaborate three-dimensional architectures that endow these structures with their durability and resistance to environmental perturbations. We used agent-based modeling to explore whether local cellular interactions were sufficient to give rise to global structural features of biofilms. Specifically, we asked whether chemorepulsion from a self-produced quorum-sensing molecule, autoinducer-2 (AI-2), was sufficient to recapitulate biofilm growth and cellular organization observed for biofilms of the human pathogen *Helicobacter pylori*. To carry out this modeling, we modified an existing platform, Individual-based Dynamics of Microbial Communities Simulator (iDynoMiCS), to incorporate three-dimensional chemotaxis, planktonic cells that could join or leave the biofilm structure, and cellular production of AI-2. We simulated biofilm growth of previously characterized *H. pylori* strains with varying AI-2 production and sensing capacities. Using biologically plausible parameters, we were able to recapitulate both the variation in biofilm mass and cellular distributions observed with these strains. Specifically, the strains that were competent to chemotax away from AI-2 produced smaller and more heterogeneously spaced biofilms, whereas the AI-2 chemotaxis defective strains produced larger and more homogeneously spaced biofilms. The model also provided new insights into the cellular demographics contributing to the biofilm patterning of each strain. Our analysis supports the idea that cellular interactions at small spatial and temporal scales are sufficient to give rise to larger scale emergent properties of biofilms.

Importance: Most bacteria exist in aggregated, three-dimensional structures called biofilms. Biofilms are resistant to antimicrobials and can pose societal problems, for example when they grow in plumbing systems or on medical implants. Understanding the processes that promote the growth and disassembly of biofilms could lead to better strategies to manage these structures. We had previously shown that *Helicobacter pylori* bacteria are repulsed by high concentrations of a self-produced molecule, autoinducer-2 (AI-2) and that *H. pylori* mutants deficient in AI-2 sensing form larger and more homogeneously spaced biofilms. Here we used computer simulations of biofilm formation to show that local *H. pylori* behavior of repulsion from high AI-2 could explain the overall architecture of *H. pylori* biofilms. Our findings demonstrate that it is possible to change global biofilm organization by manipulating local cell behaviors, which suggests that simple strategies targeting cells at local scales could be useful for controlling biofilms in industrial and medical settings.

Keywords (4-6)

Biofilms, agent-based modeling, *Helicobacter pylori*, autoinducer-2, chemotaxis

Introduction

Bacteria often exist in aggregated, adherent communities called biofilms in which the cells are encased in a self-produced matrix and adopt distinctive three-dimensional architectures with heterogeneous cell spacing that gives rise to networks of channels. These biofilm structures confer increased resistance to

environmental stressors such as antibiotics, changes in pH, and host immune defenses (1, 2). The architecture of mature biofilms contributes to their durability and resilience to perturbations by allowing for the flow of nutrients and waste products into and out of the cell aggregates (2–5). Biofilms create many commercial and biomedical problems for society, from biofouling of municipal waterworks to life-threatening infections by pathogens harbored on medical implants or the lungs of cystic fibrosis patients (1, 6, 7). Being able to understand and ultimately manipulate biofilm assembly and disassembly would help address several major industrial and biomedical challenges.

Biofilm assembly has been described alternatively as a developmental program controlled by stage-specific gene expression, similar to the development of a multicellular organism, or as the outcome of local adaptations of individual cells (8, 9). Distinguishing these two alternative possibilities is challenging because it can be difficult to discern whether biofilm phenotypes are achieved by optimizing group or individual fitness. For example, genes identified through forward genetic screens as being required for normal biofilm structures could be interpreted alternatively as being part of a biofilm genetic program or as controlling certain cellular behaviors that contribute to the self-assembly of biofilm structures. As a complement to experimental studies, computational modeling has played an important role in the study of biofilm assembly because it provides researchers with the opportunity to test and refine their understanding of the minimal set of parameters that can give rise to biofilm structures observed in nature (10–12).

A distinguishing feature of the biofilm lifestyle is that cells in close proximity can produce and respond to secreted molecular signals on small spatial and temporal scales. One such example of a secreted signal is the class of quorum-sensing molecules that serve as density-dependent forms of communication to influence group behaviors. These can include species-specific molecules, such as acylated homoserine lactones produced by many Gram-negative bacteria and perceived by species-specific receptors. Another example of a quorum-sensing molecule is the tetrahydroxy furan molecule autoinducer 2 (AI-2), which is produced by many bacteria through a common metabolic pathway but elicits different responses through species-specific receptors. Quorum-sensing molecules often regulate gene expression, including genes involved in biofilm growth and dissolution, by acting through canonical signal transduction pathways (13, 14). In this context, quorum-sensing molecules can be viewed as master regulators of biofilm developmental programs. AI-2 specifically has been shown to influence the overall structure of bacterial biofilms in diverse organisms such as *Bacillus*, *Streptococcus*, *Aggregatibacter, Pseudomonas, Escherichia, Vibrio, and Helicobacter* (15–22). In addition to regulating gene expression, AI-2 can elicit more immediate behaviors in bacteria through chemotaxis signal transduction that directs bacterial movement relative to a chemical gradient (16, 23–27). In the case of *Helicobacter pylori*, we showed that AI-2 is perceived as a chemorepellent (28), whereas *Escherichia coli* perceives AI-2 as a chemoattractant (25).

Previous experimental work from our group showed that both *H. pylori* biofilm mass and structural patterning are influenced by AI-2 chemotaxis. To determine the role of AI-2 in *H. pylori* biofilm formation, we constructed strains that were defective for AI-2 production *(luxS*$^{-}$), AI-2 chemoreception (*cheA*$^{-}$*, tlpB*$^{-}$*, aibA*$^{-}$*, aibB*$^{-}$), or overproduced AI-2 (*luxS*^{OP}). We measured the biomass of the resulting biofilms using a crystal violet assay. We also measured the structural heterogeneity of the resulting biofilms by imaging them with fluorescence microscopy and quantifying a lacunarity metric that captures morphological features such as roughness of biofilm edges and patchiness of surface coverage. We observed that both AI-2 sensing and production mutants formed larger biofilms with more homogenous organization, whereas the strain that overproduced AI-2 formed smaller, more heterogeneously structured biofilms (16).

Our experimental observations are consistent with a role for AI-2 chemorepulsion in shaping biofilm structure. For example, bacterial cells that chemotax away from AI-2 would be motivated to leave and deterred from joining a biofilm that is a concentrated source of AI-2. Our experimental results, however, could not rule out the possibility that additional functions of AI-2 signaling, such as regulation of global gene expression programs, contribute to the overall architecture of *H. pylori* biofilms. Here we used agent-based modeling to ask whether individual cellular behaviors of AI-2 production and chemotaxis are sufficient to produce global features of biofilm structures observed experimentally.

137 To explore the extent to which AI-2 chemotactic responses could explain
138 our experimental observations, we used a well-established biofilm modeling
139 platform, Individual-based Dynamics of Microbial Communities Simulator
140 (iDynoMiCS) (29), which simulates behaviors of individual bacterial cells to
141 understand larger, community behaviors. We implemented several critical
142 modifications to iDynoMiCS in order to explore whether AI-2 chemotactic
143 responses could recapitulate our experimentally observed biofilms. First, we
144 expanded the models to include three spatial dimensions. Next, we included a
145 population of planktonic (free swimming) cells that were continually introduced
146 into the bulk medium and could join the biofilm. Additionally, cells from the biofilm
147 could leave and become part of the planktonic population. Finally, we introduced
148 AI-2 as a compound that was produced by individual cells as a function of their
149 metabolic capacity and that diffused through the three dimensional space.
150 With the addition of AI-2 production and chemoreception to our modeling
151 platform, we recapitulated our previous experimental data showing that biofilms
152 of strains lacking the ability to produce or sense AI-2 were larger than wild type
153 biofilms. In addition, the architecture of the biofilms, including spacing of cell
154 groups within the biofilms, matched well between the experimental and modeled
155 biofilms. Finally, our modeling of biofilms contributed new insight into the
156 demographics dictating biofilm size, suggesting that cell dispersal is a major
157 contributor to the reduced biofilm mass of AI-2-responsive versus non-responsive
158 cells. These results indicate the utility of our modified iDynoMiCS platform for
159 studying chemotaxis in biofilm dynamics and provide support for the view that

160 local cellular behaviors of AI-2 chemotaxis can explain global features of biofilm
161 formation and patterning.
162
163 **Materials and Methods**
164 Computational modeling of biofilms
165 The simulation of the growth of biofilms was accomplished using the
166 agent-based modeling package iDynoMiCs. Individual cells are represented as
167 discrete spherical agents with programmable behaviors that are subject to
168 influence from other agents and their surrounding environments. The model
169 consists of an evenly spaced grid of three dimensions with two compartments –
170 the bulk and the bacterial. The bulk compartment at the top represents well-
171 mixed bulk solutes that interface with the bacterial compartment at the bottom
172 through a diffusion liquid boundary layer. Solutes are represented by
173 concentration fields changing due to diffusion and from uptake by the cells in the
174 bacterial compartment that provides a surface for initial seed cells to attach. As
175 the cells uptake solutes, they can grow and divide or die above or below certain
176 set size thresholds. These processes of growth and division lead to mechanical
177 stress between the cells, which is relieved through a shoving algorithm. This
178 shoving and the simulation of other physical forces on the biofilm dictate the
179 formation of the biofilm's structure.
180 To represent a bacterial population with both biofilm-attached cells and
181 planktonic cells and to simulate the dynamics of cells joining and leaving a
182 biofilm, we extended iDynoMiCs to include new agents with attributes and

behaviors specific to planktonic cells. This version is available at https://github.com/alexwweston/iDynoMiCS. Cells can be either biofilm-associated or planktonic cells capable of movement in two or three dimensions. A set number of planktonic cells are introduced into the simulation from the bulk compartment at a chosen interval and removed from the simulation if they leave the boundaries of the bacterial compartment. An individual planktonic cell will move at a random distance between 0 and its maximum distance at a random angle. If it ends its movement within a certain distance from a biofilm-associated cell, it will then switch from planktonic to biofilm-associated behaviors. The maximum distance to move and the threshold distance for joining a biofilm are simulation parameters.

Planktonic cells are also given behaviors to simulate chemotaxis response. A chemotaxing planktonic cell has attributes from the solute it identifies as a chemoeffector, whether or not it exhibits an attractive or repellent response to this chemoeffector, and the threshold for recognizing this chemoeffector. Before moving, a planktonic cell will detect the concentration of its chemoeffector at its current location. If it is above its chemoeffector threshold, it will detect the gradient of the chemoeffector and move at an angle towards or away from this gradient depending on its response.

The attributes and behaviors of biofilm-associated cells are additionally extended to simulate biofilm-associated cells leaving the biofilm and becoming planktonic. A biofilm-associated cell has attributes for its chemoeffector, a threshold for recognizing this chemoeffector, and a probability for leaving the

biofilm if this threshold is surpassed. At the end of each interval in the simulation, cells on the periphery of the biofilm will check the local concentrations of their chemoeffector. If the concentration is above its chemoeffector threshold, that cell has a chance of leaving the biofilm at a frequency equal to its leaving probability. Upon leaving the biofilm, that cell becomes a planktonic cell and moves from the biofilm at a random angle away from the chemoeffector gradient. The chosen chemotaxis threshold corresponds to the concentration of AI-2 at which planktonic cells contribute to the population of the biofilm at the midpoint between cells never joining the biofilm and cells always joining the biofilm (Supplemental Figure 1).

To model the production of AI-2 by the cells, we examined multiple AI-2 production regimes, each creating different concentrations and localization patterns of AI-2 in the model biofilms. These three regimes included: constitutive production of AI-2, production of AI-2 tied to the growth reaction, and production of AI-2 tied to the growth reaction with additional update of AI-2 by the cells. Although the distribution of the AI-2 molecule within a biofilm is unknown, we measured the total concentration of AI-2 at different time points in *H. pylori* biofilms and compared these results with the total concentrations of AI-2 generated in our simulations under the different regimes (data not shown). From these results, we chose to model AI-2 production where it was tied to the growth reaction with uptake by the cells.

229 Setting up and running simulations

230 We simulated the movement of bacteria through a 280x280x280 μm
231 space for a period of 24 h. The space was modeled as a 33x33x33 grid. Fluid
232 movement was simulated using a major time step size of 1.0 h, and bacterial
233 behaviors (movement, joining, leaving) were updated at minor time steps of 0.05
234 h. Each simulation was seeded with 100 bacteria cells randomly placed on the
235 bottom layer of the simulated grid. Outputs for visualization were recorded at the
236 end of every major time step. Other parameters for concentration and diffusivity
237 of solutes and the cell attributes of agents were taken from measurements of *E.*
238 *coli* biofilms used in other simulations under iDynoMiCs. Erosion and sloughing
239 processes that can be modeled in iDynoMiCs were turned off for these
240 simulations. A full list of these parameters that were static in our simulations is
241 available in Supplementary Table 1.

242 Parameters that were introduced in this new model were tested across a
243 wide variety of ranges and values were chosen where moderate behavior was
244 observed. Microbial growth kinetics were modeled using the Monod growth
245 equation with an additional term representing the production of AI-2. The values
246 for these parameters and equations for the wild type strain used in the
247 simulations are found on Supplementary Table 2. Mutant strains used in the
248 simulations use minor modifications of these values, which are highlighted on
249 Supplementary Table 3. The mutant chemotaxis strain is given an infinite value
250 for its chemotaxis threshold causing it to never detect its chemoeffector, the
251 mutant overproducer strain is given a larger AI-2 yield coefficient, and the mutant

252 strain defective in AI-2 production creates an arbitrary alternative product other
253 than AI-2 from its growth reaction.
254
255 Visualizing the biofilms
256 The visualization of the agent-based simulation of gut microbes was
257 created using custom-built codes developed in C++, using OpenGL for the
258 graphics and Qt for the user interface. The simulations are run within iDynoMiCS,
259 which exports the entirety of the simulation in XML. Each microbe is displayed as
260 a sphere that has a radius dictated by the simulation and a color based on the
261 microbe type, and in some scenarios, modified based on family, genealogy,
262 generation, or birthday. Each founding cell is labeled in a different shade of pink
263 and the daughter cells remain the same color as the original founding cell to
264 allow for recognition of clones. The code is open source and can be downloaded
265 at https://bitbucket.org/kpotter/vizr.
266 The visualization of the AI-2 gradients via contours was done using the R
267 library filled.contours. To create these images, the data is loaded into R, a single
268 slice of the data volume is extracted at a specified timepoint, and this data is
269 used as input to the contours function. The R code is provided in Supplemental
270 Materials and Methods.
271
272 Calculating lacunarity
273 The simulated biofilms all become 100% confluent by 24 h. To compare
274 more directly to the experimental biofilms, which were often not confluent by 24

h, a bottom portion of each simulated biofilm was removed. To decide how much to trim off, the percent cell coverage across all experimental wild type images was determined to be approximately 43% percent coverage using ImageJ. Removing the bottom 98 μm from the simulated biofilms resulted in 43% coverage for a representative set of wild type biofilms, viewed from the top down (Figure 4A). Therefore, 98 μm was removed from all simulated biofilms and lacunarity was determined. To determine the lacunarity score, we opened the experimental or trimmed simulated biofilm images in ImageJ, converted them to black and white, adjusted the threshold to a set cutoff, and analyzed the resultant images using the FracLac plugin.

Results

Addition of chemotaxis and AI-2 production to agent-based modeling of biofilm formation

Agent-based models are useful tools for exploring how simple interactions between cells contribute to the overall properties of bacterial communities, such as biofilms. iDynoMiCS simulates biofilm formation by taking into account biologically relevant parameters such as nutrient concentrations, nutrient diffusion rates, and cell division and spacing [see Supplementary table 1 for parameters used in the simulation (29)]. To investigate the role of AI-2 mediated chemotaxis in biofilm architecture, we extended the iDynoMiCS model by introducing several properties, including: three-dimensional chemotaxis,

298 planktonic (free swimming) cells, cells joining and leaving the biofilm, and AI-2
299 production. These new iDynoMiCS additions were critical for exploring how
300 chemoreception of AI-2 shapes *H. pylori* biofilms. In addition, these
301 developments necessitated a new visualization tool that aided in data
302 interpretation (see Materials and Methods).

303 Our extended model starts with 100 bacterial cells randomly placed on the
304 two-dimensional surface at the bottom of a container that is continually supplied
305 with fresh, nutrient-containing medium. These cells expand and proliferate
306 according to the iDynoMICS growth and spacing algorithms. We allowed new
307 planktonic cells to enter the container throughout each 24 h simulation (Figure 1A
308 and Supplementary movies). The planktonic cells moved through the space
309 according to a chemotaxis algorithm (see Materials and Methods). Planktonic
310 cells would join the simulated biofilm if they swam close enough to the biofilm
311 surface and if the concentration of a chemorepellant was below a set threshold.
312 In addition, cells at the biofilm edge could leave and enter into the planktonic
313 pool. In our simulations, we chose the AI-2 chemotaxis threshold to be that at
314 which planktonic cells contributed to the population of the biofilm to the extent
315 that was defined as halfway between cells never joining the biofilm and cells
316 always joining the biofilm (Supplemental Figure 1).

317 After testing several models of AI-2 production (see Materials and
318 Methods), we chose a model that tied AI-2 production directly to the growth and
319 metabolism of each cell or agent. This model is reasonable because AI-2 is
320 produced as a by-product of the activated methyl cycle (30). We also

incorporated into the model a constant cellular uptake of AI-2, which is common in bacteria (31). We do not yet know whether *H. pylori* has an active AI-2 uptake mechanism, but incorporating a constant uptake parameter best recapitulated our experimental measurements of AI-2 [(16, 23) and data not shown]. In the iDynomics simulations, cells near the surface of the modeled biofilms have more access to fresh nutrients and therefore divide and produce AI-2 at a higher rate than cells in the middle or bottom of the biofilm (Figure 1B). The constant cellular uptake of AI-2 in the model resulted in a lower concentration of AI-2 in the volume just below the surface of the biofilm (Figure 1B).

Modeling recapitulates biofilm mass as a function of AI-2 chemorepulsion

Using the model, we tested whether we could recapitulate the outcomes of our previous experiments demonstrating an important role for AI-2 production and chemorepulsion in *H. pylori* biofilm mass and patterning (16). To simulate these experiments, we modeled the strains and conditions used in this experimental work. The strains included wild type cells, cells unable to chemotax, cells unable to produce AI-2, and cells that overproduce AI-2. For each of these genotypes we ran 30 individual iterations and compared the number of cells in our simulated *H. pylori* biofilms to those of experimental work (Figure 2). Wild type cells produced moderately sized biofilms in both the model and the experimental set-up, while cells that could not produce AI-2 or chemotax away from AI-2 produced larger biofilms. Finally, both experimental and modeling results revealed that the AI-2 overproducer made smaller biofilms. This data

344 served as confirmation that our modeling platform could recapitulate
345 experimental results.
346
347 ***Modeling predicts subcellular populations that contribute to biofilm mass***
348 The model afforded us the opportunity to examine the cellular
349 demographics contributing to biofilm mass, which would be difficult to do
350 experimentally. We modeled biofilm formation for 24 h in 30 parallel simulations
351 and tallied the individual leaving events and joining events. Wild type biofilms
352 showed equivalent numbers of joining and leaving cells (Figure 3). As expected,
353 biofilms of non-chemotactic and AI-2 non-producing cells had no leaving events,
354 since AI-2 chemorepulsion was the only leaving mechanism in the model. The
355 AI-2 over-producer strain had a dramatic increase of leaving events, which was
356 expected given the higher concentration of AI-2 near the surface of the biofilm
357 (Figure 2B) that would drive cells to chemotax away from the biofilm.
358 Interestingly, both the non-chemotactic and AI-2 non-producers had a reduction
359 in the number of joining events as compared to the wild type population, despite
360 not experiencing chemorepulsion from the biofilm. Also counter-intuitively there
361 were more overall joining events in the AI-2 over-producer strain biofilm than in
362 the wild type population. As discussed below, the number of joiners could be
363 explained by the differences in architectures and specifically surface areas and
364 joining opportunities afforded by the growing biofilms of the different strains.
365 Overall, our modeling supports the idea that AI-2 chemorepulsion promotes a
366 balance of leaving and joining events that influences the global biofilm size.

Modeling recapitulates the impact of AI-2 chemorepulsion on biofilm spatial organization

Finally, we used modeling to confirm that AI-2 shapes *H. pylori* biofilm architecture. We had shown previously that we could quantify the heterogeneity of biofilms using a lacunarity metric, which measures spacing between patterns and boundary smoothness. Experimental biofilms were grown on glass slides, fixed and stained with DAPI and visualized with epifluorescence. The cellular component of the biofilm was defined using an intensity threshold and the resulting images were analyzed using an ImageJ plugin, FracLac, to quantify lacunarity [Figure 4, (32–34)]. We took 10 simulated biofilms for each genotype and performed a similar analysis of a top view of the structure (Figure 4A). Visually, the simulated biofilm structures (Figure 4B) resembled the experimental data (Figure 4C). The wild type and AI-2 overexpressing strains produced biofilms with marked spacing between cell patches, whereas the non-chemotactic and AI-2 non-producing strains formed much more homogeneous structures. Plotting the resulting lacunarity scores revealed a striking similarity between experimental and modeling data (Figure 4D and E).

Discussion

In this study, we used agent-based modeling to explore whether local cell chemotaxic responses to a self-produced molecule could explain biofilm growth and patterning properties. By extending the iDynoMiCS modeling platform to

include three-dimensional chemotaxis, cell joining and leaving events, and AI-2 production, we were able to recapitulate our experimental observations of *H. pylori* biofilm formation with a collection of strains with different AI-2 production and perception properties (16). We showed that cells unable to make or chemotax away from AI-2 produced larger biofilms than wild type cells. These biofilms also differed in their organization with more homogenous cell spacing and smaller gaps between cell clusters. Over-production of AI-2 resulted in smaller and more heterogeneously spaced biofilms. Mature biofilms are complex structures with towers and channels that facilitate fluid flow for efficient oxygen and nutrient permeation, waste excretion, and cell turnover (2–5). We found that by modeling local chemotactic responses to a self-produced molecule, we could simulate the assembly of biofilms with the global property of high lacunarity, characteristic of biofilms with extensive channels (Figure 4). The agreement between our simulations and experimental results supports the idea that local cellular behaviors, such as production and chemoavoidance of AI-2, can explain global architectural features of bacterial biofilms.

Our modeling approach allowed us to dissect the demographics of biofilm assembly in a way that would be difficult to do experimentally without sophisticated genetic tools for marking cell lineages. As expected, in our model cells left the biofilm when they were programmed to chemotax away from AI-2, and they left in greater numbers when the biofilm cells produced more AI-2. We did not initially expect the wild type and AI-2 overproducer populations to have more cells join the biofilms than the populations without chemotaxis or AI-2

413 production. However, inspection of the biofilm structures assembled in these
414 different models showed that the wild type and overproducer biofilms had many
415 more gaps and edges, creating more extensive surface area that planktonic cells
416 would stochastically encounter and then join at a certain probability. This
417 difference in surface area and joining opportunities could explain the higher
418 numbers of joiners in the populations of cells engaging in AI-2 chemorepulsion.
419 In addition, the heterogeneous architectures of these biofilms would create local
420 minima in AI-2 concentrations and opportunities for joining even in the context of
421 AI-2 chemorepulsion. Differences in the local AI-2 concentration landscapes
422 could explain the higher number of joiners seen with the AI-2 overproducer
423 versus wild type cell populations.

424 Although our model recapitulated several features of AI-2 dependent
425 biofilm assembly observed experimentally, it is based on certain assumptions
426 about AI-2 fluxes that are likely to be oversimplifications. In our current model, AI-
427 2 production is linked to metabolic activity and uptake is constant. When
428 examined experimentally, parameters of AI-2 production, uptake and sensing are
429 known to vary greatly between bacterial species and depending on cells'
430 metabolic states (35–38). Using deterministic simulations of AI-2 production from
431 a system of ordinary differential equations, Quan and colleagues showed that
432 variability in AI-2 uptake within a modeled biofilm can lead to desynchronization
433 of autoinduction across the community (39), highlighting the importance of
434 considering heterogeneities in AI-2 fluxes. In addition, AI-2 could be produced
435 from sources other than the bacterial constituents of a biofilm. For example,

436 mammalian host tissues were recently shown to synthesize an AI-2 mimic that is
437 sensed by bacterial AI-2 receptors (40). Future iterations of the model could
438 incorporate more detailed parameters of AI-2 fluxes, but these would need to be
439 tailored to the specific bacterial species and environments being modeled.

440 Most bacteria exist not in mono-cultures but rather in multi-species
441 consortia (41). AI-2 is known to contribute to the organization of such consortia,
442 for example in biofilms that assemble on the enamel surfaces of teeth (42, 43).
443 Recently, Laganenka and Sourjik showed that in a simple two-member biofilm
444 community of *Enterococcus faecalis* and *Escherichia coli* cells, AI-2 chemotaxis
445 plays an important role in biofilm growth and patterning. In this model community,
446 both species produce AI-2 but only *E. coli* chemotaxes toward it (27). It would be
447 interesting to apply our modeling approach to this experimental system to test
448 whether it would recapitulate observed architectural features, such as the spatial
449 segregation of *E. faecalis* and *E. coli* cells. More generally, by applying our
450 modeling approach to complex multi-species communities and assigning simple
451 AI-2 production, chemoattraction, and chemorepulsion behaviors to different
452 members, one could explore the extent to which local AI-2 chemotactic
453 responses could explain global spatial patterning observed in multi-species
454 communities.

455

456 **Acknowledgements**

457 Research reported in this publication was supported by the National Institute of
458 Diabetes and Digestive and Kidney Diseases and the National Institute of

General Medical Sciences of the National Institutes of Health under award numbers R01DK101314 and P50GM098911 (to K.G.) and the Medical Research Foundation Oregon Scientist Development Award (to E.G.S). The content is solely the responsibility of the authors and does not necessarily represent the official views of the National Institutes of Health.

Figure Legends

Figure 1. Time steps and AI-2 gradients of example wild type iDynoMiCS modeled *H. pylori* biofilm. A) Wild type biofilm after 2, 16 and 24 h of growth. Each sphere represents a modeled bacterial cell with colors corresponding to different cell behaviors (see legend). Note there is a mix of cells leaving, dividing from the original founding population and cells joining the biofilm. Each grouping of pink cells represents a clonal population. B) Shown are corresponding AI-2 concentration graphics below each time point shown in A. The AI-2 concentration is a representative vertical slice through the center of the 3D modeled biofilm, with darker color representing higher concentrations of AI-2.

Figure 2. Modeling confirms AI-2 chemotaxis and production alter overall biofilm size. A) Representative images of 24 h biofilms for each of the four strains in grayscale to show contours. To simplify, only the founding population, their progeny and joiners are shown. Planktonic cells have been removed for simplicity. B) The associated AI-2 gradients for panels in A. C) Total number of cells attached to the modeled biofilms at timepoint 24 h. n = 30 D) The size of the

482 experimental biofilms from Anderson et al. are graphed according to percentage
483 of cells in the biofilm (compared to planktonic). Stars indicate a significant
484 difference from wild type. Statistics for C and D were determined using a one-
485 way analysis of variance ($p < 0.05$). 2D data from Anderson et al. 2015 (16).
486
487 **Figure 3. Modeling confirms AI-2 chemotaxis and production influence the**
488 **behavior of the cells in the biofilm.** Each leaving and joining event from 0-24 h
489 of the modeled biofilms was graphed by genotype. Stars indicate a significant
490 difference, results determined using a one-way analysis of variance ($p < 0.05$). n
491 = 30 biofilms
492
493 **Figure 4. Modeling confirms AI-2 chemotaxis and production influence**
494 **biofilm organization.** A) Lacunarity analysis pipeline for the modeled biofilm
495 images. Bottom 98 μm removed from each 24 h biofilm across all genotypes (see
496 Materials and Methods). The top-down view is used to be able to compare to the
497 experimental images (4C). Using ImageJ, each image was thresholded and then
498 run through FracLac to determine the lacunarity score. More details can be found
499 in the Materials and Methods section. B) Example images of all four modeled
500 genotypes from the top-down. C) Example images of experimental *H. pylori*
501 biofilms grown on glass slides, from Anderson et al. 2015. D) Lacunarity scores
502 graphed for modeled biofilms (n = 8-10). E) Lacunarity scores graphed for each
503 experimental biofilm for each genotype from Anderson et al. Stars in D and E

indicate a significant difference from wild type, results determined using a one-way analysis of variance ($p < 0.05$). 4E data from Anderson et al. 2015 (16).

References

1. Gupta P, Sarkar S, Das B, Bhattacharjee S, Tribedi P. 2016. Biofilm, pathogenesis and prevention—a journey to break the wall: a review. Arch Microbiol 198:1–15.

2. Hall-Stoodley L, Costerton JW, Stoodley P. 2004. Bacterial biofilms: from the Natural environment to infectious diseases. Nat Rev Microbiol 2:95–108.

3. Melaugh G, Hutchison J, Kragh KN, Irie Y, Roberts A, Bjarnsholt T, Diggle SP, Gordon VD, Allen RJ. 2016. Shaping the Growth Behaviour of Biofilms Initiated from Bacterial Aggregates. PloS One 11:e0149683.

4. Stewart PS. 2012. Mini-review: convection around biofilms. Biofouling 28:187–198.

5. Wilking JN, Zaburdaev V, De Volder M, Losick R, Brenner MP, Weitz DA. 2013. Liquid transport facilitated by channels in Bacillus subtilis biofilms. Proc Natl Acad Sci U S A 110:848–852.

6. Aparna MS, Yadav S. 2008. Biofilms: microbes and disease. Braz J Infect Dis Off Publ Braz Soc Infect Dis 12:526–530.

7. Nguyen T, Roddick FA, Fan L. 2012. Biofouling of Water Treatment Membranes: A Review of the Underlying Causes, Monitoring Techniques and Control Measures. Membranes 2:804–840.

525 8. Klausen M, Gjermansen M, Kreft J-U, Tolker-Nielsen T. 2006. Dynamics of
526 development and dispersal in sessile microbial communities: examples from
527 Pseudomonas aeruginosa and Pseudomonas putida model biofilms. FEMS
528 Microbiol Lett 261:1–11.

529 9. Monds RD, O'Toole GA. 2009. The developmental model of microbial
530 biofilms: ten years of a paradigm up for review. Trends Microbiol 17:73–87.

531 10. Ghanbari A, Dehghany J, Schwebs T, Müsken M, Häussler S, Meyer-
532 Hermann M. 2016. Inoculation density and nutrient level determine the
533 formation of mushroom-shaped structures in *Pseudomonas aeruginosa*
534 biofilms. Sci Rep 6:32097.

535 11. Nadell CD, Drescher K, Foster KR. 2016. Spatial structure, cooperation and
536 competition in biofilms. Nat Rev Microbiol 14:589–600.

537 12. Pérez-Velázquez J, Gölgeli M, García-Contreras R. 2016. Mathematical
538 Modelling of Bacterial Quorum Sensing: A Review. Bull Math Biol 78:1585–
539 1639.

540 13. Papenfort K, Bassler BL. 2016. Quorum sensing signal-response systems in
541 Gram-negative bacteria. Nat Rev Microbiol 14:576–588.

542 14. Vendeville A, Winzer K, Heurlier K, Tang CM, Hardie KR. 2005. Making
543 "sense" of metabolism: autoinducer-2, LuxS and pathogenic bacteria. Nat
544 Rev Microbiol 3:383–396.

15. Ali SA, Benitez JA. 2009. Differential response of Vibrio cholerae planktonic and biofilm cells to autoinducer 2 deficiency. Microbiol Immunol 53:582–586.

16. Anderson JK, Huang JY, Wreden C, Sweeney EG, Goers J, Remington SJ, Guillemin K. 2015. Chemorepulsion from the Quorum Signal Autoinducer-2 Promotes *Helicobacter pylori* Biofilm Dispersal. mBio 6:e00379-15.

17. Auger S, Krin E, Aymerich S, Gohar M. 2006. Autoinducer 2 affects biofilm formation by Bacillus cereus. Appl Environ Microbiol 72:937–941.

18. Li H, Li X, Wang Z, Fu Y, Ai Q, Dong Y, Yu J. 2015. Autoinducer-2 regulates Pseudomonas aeruginosa PAO1 biofilm formation and virulence production in a dose-dependent manner. BMC Microbiol 15:192.

19. Li J, Attila C, Wang L, Wood TK, Valdes JJ, Bentley WE. 2007. Quorum sensing in Escherichia coli is signaled by AI-2/LsrR: effects on small RNA and biofilm architecture. J Bacteriol 189:6011–6020.

20. Niu C, Robbins CM, Pittman KJ, Osborn joDi L, Stubblefield BA, Simmons RB, Gilbert ES. 2013. LuxS influences Escherichia coli biofilm formation through autoinducer-2-dependent and autoinducer-2-independent modalities. FEMS Microbiol Ecol 83:778–791.

21. Novak EA, Shao H, Daep CA, Demuth DR. 2010. Autoinducer-2 and QseC control biofilm formation and in vivo virulence of Aggregatibacter actinomycetemcomitans. Infect Immun 78:2919–2926.

565 22. Wang Z, Xiang Q, Yang T, Li L, Yang J, Li H, He Y, Zhang Y, Lu Q, Yu J.
566 2016. Autoinducer-2 of Streptococcus mitis as a Target Molecule to Inhibit
567 Pathogenic Multi-Species Biofilm Formation In Vitro and in an Endotracheal
568 Intubation Rat Model. Front Microbiol 7:88.

569 23. Rader BA, Campagna SR, Semmelhack MF, Bassler BL, Guillemin K. 2007.
570 The Quorum-Sensing Molecule Autoinducer 2 Regulates Motility and
571 Flagellar Morphogenesis in Helicobacter pylori. J Bacteriol 189:6109–6117.

572 24. Laganenka L, Colin R, Sourjik V. 2016. Chemotaxis towards autoinducer 2
573 mediates autoaggregation in Escherichia coli. Nat Commun 7:12984.

574 25. Hegde M, Englert DL, Schrock S, Cohn WB, Vogt C, Wood TK, Manson MD,
575 Jayaraman A. 2011. Chemotaxis to the quorum-sensing signal AI-2 requires
576 the Tsr chemoreceptor and the periplasmic LsrB AI-2-binding protein. J
577 Bacteriol 193:768–773.

578 26. Jani S, Seely AL, Peabody V GL, Jayaraman A, Manson MD. 2017.
579 Chemotaxis to self-generated AI-2 promotes biofilm formation in Escherichia
580 coli. Microbiology 163:1778–1790.

581 27. Laganenka L, Sourjik V. 2018. Autoinducer 2-Dependent Escherichia coli
582 Biofilm Formation Is Enhanced in a Dual-Species Coculture. Appl Env
583 Microbiol 84:e02638-17.

584 28. Rader BA, Wreden C, Hicks KG, Sweeney EG, Ottemann KM, Guillemin K.
585 2011. Helicobacter pylori perceives the quorum-sensing molecule AI-2 as a

586 chemorepellent via the chemoreceptor TlpB. Microbiol Read Engl 157:2445–
587 2455.

588 29. Lardon LA, Merkey BV, Martins S, Dötsch A, Picioreanu C, Kreft J-U, Smets
589 BF. 2011. iDynoMiCS: next-generation individual-based modelling of
590 biofilms: iDynoMiCS for Biofilm Modelling. Environ Microbiol 13:2416–2434.

591 30. Vendeville A, Winzer K, Heurlier K, Tang CM, Hardie KR. 2005. Making
592 “sense” of metabolism: autoinducer-2, LuxS and pathogenic bacteria. Nat
593 Rev Microbiol 3:383–396.

594 31. Weiland-Bräuer N, Pinnow N, Schmitz RA. 2015. Novel reporter for
595 identification of interference with acyl homoserine lactone and autoinducer-2
596 quorum sensing. Appl Environ Microbiol 81:1477–1489.

597 32. Karperien A, Ahammer H, Jelinek HF. 2013. Quantitating the subtleties of
598 microglial morphology with fractal analysis. Front Cell Neurosci 7:3.

599 33. Schneider CA, Rasband WS, Eliceiri KW. 2012. NIH Image to ImageJ: 25
600 years of image analysis. Nat Methods 9:671–675.

601 34. Tolle C, McJunkin T, Rohrbaugh D, LaViolette R. 2003. Lacunarity definition
602 for ramified data sets based on optimal cover. Phys D Non-linear Phenom
603 179:129–152.

604 35. Mitra A, Herren CD, Patel IR, Coleman A, Mukhopadhyay S. 2016.
605 Integration of AI-2 Based Cell-Cell Signaling with Metabolic Cues in
606 Escherichia coli. PloS One 11:e0157532.

607 36. Xavier KB, Bassler BL. 2005. Regulation of uptake and processing of the
608 quorum-sensing autoinducer AI-2 in Escherichia coli. J Bacteriol 187:238–
609 248.

610 37. Surette MG, Miller MB, Bassler BL. 1999. Quorum sensing in Escherichia
611 coli, Salmonella typhimurium, and Vibrio harveyi: A new family of genes
612 responsible for autoinducer production. Proc Natl Acad Sci U S A 96:1639–
613 1644.

614 38. Hardie KR, Heurlier K. 2008. Establishing bacterial communities by “word of
615 mouth”: LuxS and autoinducer 2 in biofilm development. Nat Rev Microbiol
616 6:635–643.

617 39. Quan DN, Tsao C-Y, Wu H-C, Bentley WE. 2016. Quorum Sensing
618 Desynchronization Leads to Bimodality and Patterned Behaviors. PLoS
619 Comput Biol 12:e1004781.

620 40. Ismail AS, Valastyan JS, Bassler BL. 2016. A Host-Produced Autoinducer-2
621 Mimic Activates Bacterial Quorum Sensing. Cell Host Microbe 19:470–480.

622 41. Mark Welch JL, Rossetti BJ, Rieken CW, Dewhirst FE, Borisy GG. 2016.
623 Biogeography of a human oral microbiome at the micron scale. Proc Natl
624 Acad Sci U S A 113:E791-800.

625 42. Cuadra-Saenz G, Rao DL, Underwood AJ, Belapure SA, Campagna SR,
626 Sun Z, Tammariello S, Rickard AH. 2012. Autoinducer-2 influences
627 interactions amongst pioneer colonizing streptococci in oral biofilms.
628 Microbiology 158:1783–1795.

629 43. Kolenbrander PE, Jr RJP, Periasamy S, Jakubovics NS. 2010. Oral
630 multispecies biofilm development and the key role of cell–cell distance. Nat
631 Rev Microbiol 8:471–480.

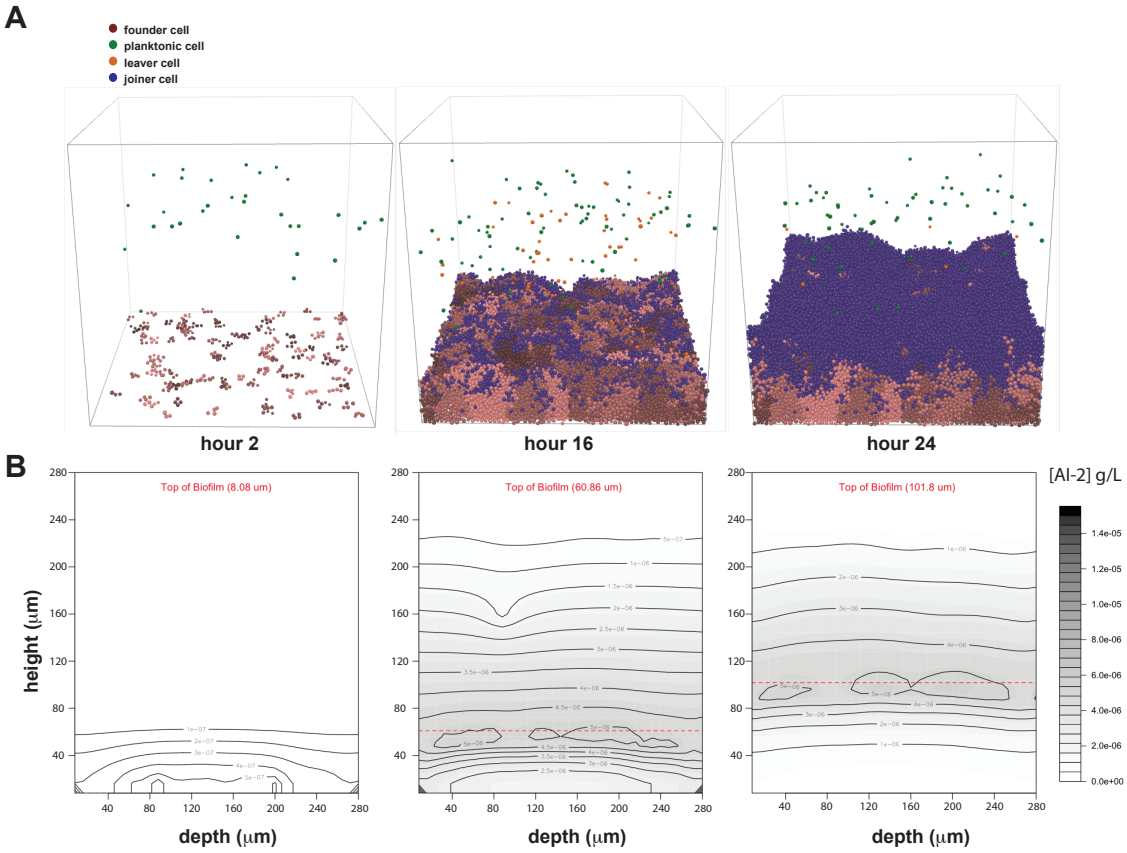

Figure 1. Time steps and AI-2 gradients of example wild type iDynoMiCS modeled *H. pylori* biofilm. A) Wild type biofilm after 2, 16 and 24 h of growth. Each sphere represents a modeled bacterial cell with colors corresponding to different cell behaviors (see legend). Note there is a mix of cells leaving, dividing from the original founding population and cells joining the biofilm. Each grouping of pink cells represents a clonal population. B) Shown are corresponding AI-2 concentration graphics below each time point shown in A. The AI-2 concentration is a representative vertical slice through the center of the 3D modeled biofilm, with darker color representing higher concentrations of AI-2.

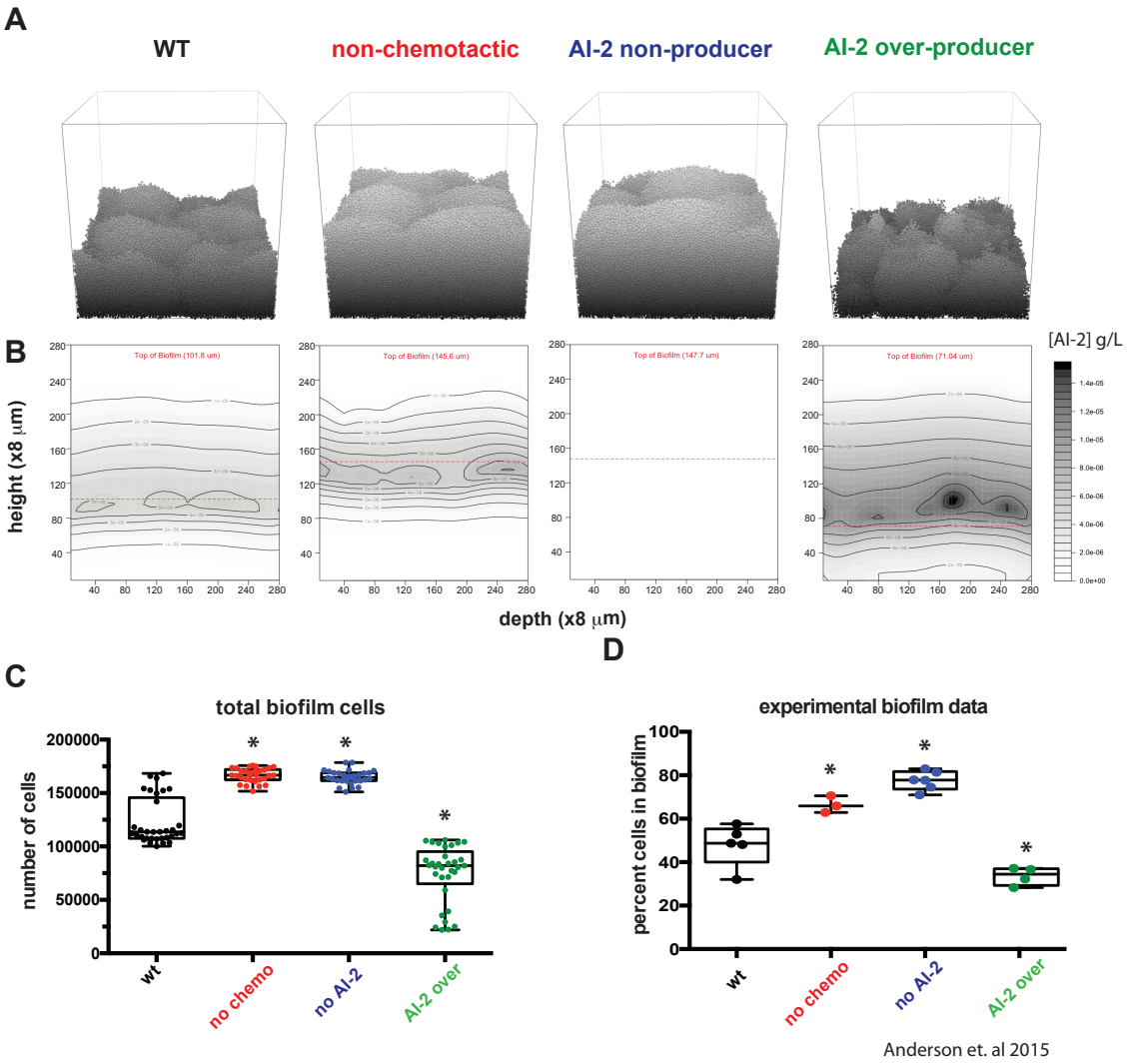

Figure 2. Modeling confirms AI-2 chemotaxis and production alter overall biofilm size. A) Representative images of 24 h biofilms for each of the four strains in grayscale to show contours. To simplify, only the founding population, their progeny and joiners are shown. Planktonic cells have been removed for simplicity. B) The associated AI-2 gradients for panels in A. C) Total number of cells attached to the modeled biofilms at timepoint 24 h. n = 30 D) The size of the experimental biofilms from Anderson et al. are graphed according to percentage of cells in the biofilm (compared to planktonic). Stars indicate a significant difference from wild type. Statistics for C and D were determined using a one-way analysis of variance ($p < 0.05$). 2D data from Anderson et al. 2015 (16).

633

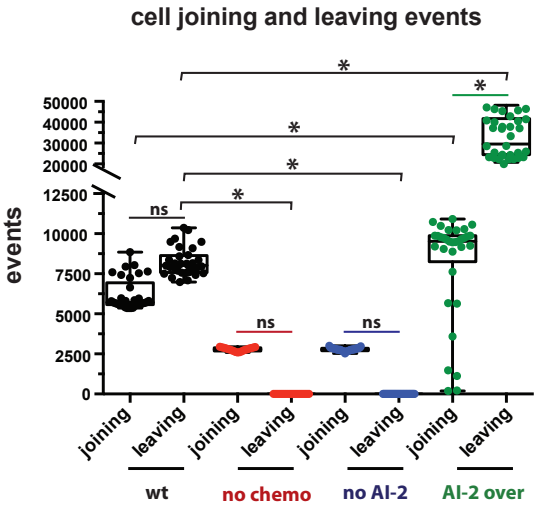

Figure 3. Modeling confirms AI-2 chemotaxis and production influence the behavior of the cells in the biofilm. Each leaving and joining event from 0-24 h of the modeled biofilms was graphed by genotype. Stars indicate a significant difference, results determined using a one-way analysis of variance ($p < 0.05$). n = 30 biofilms

634

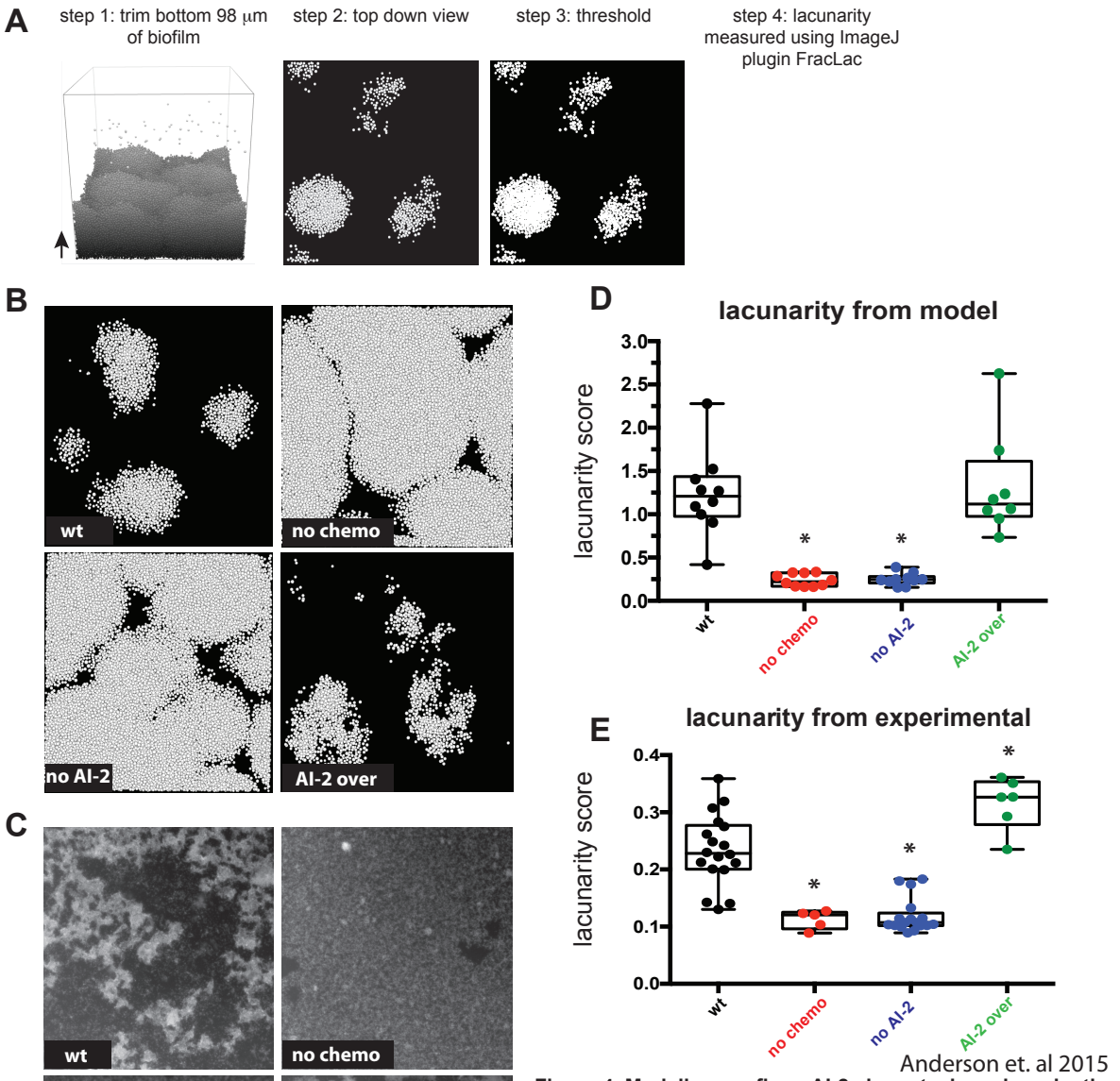

Figure 4. Modeling confirms AI-2 chemotaxis and production influence biofilm organization. A) Lacunarity analysis pipeline for the modeled biofilm images. Bottom 98 mm removed from each 24 h biofilm across all genotypes (see Materials and Methods). The top-down view is used to be able to compare to the experimental images (4C). Using ImageJ, each image was thresholded and then run through FracLac to determine the lacunarity score. More details can be found in the Materials and Methods section. B) Example images of all four modeled genotypes from the top-down. C) Example images of experimental *H. pylori* biofilms grown on glass slides, from Anderson et al. 2015. D) Lacunarity scores graphed for modeled biofilms (n = 8-10). E) Lacunarity scores graphed for each experimental biofilm for each genotype from Anderson et al. Stars in D and E indicate a significant difference from wild type, results determined using a one-way analysis of variance ($p < 0.05$). 4E data from Anderson et al. 2015 (16).

635